SANDIA REPORT
SAND2017-11076
Unlimited Release
Printed October, 2017

Emergent Phenomena in Oxide Nanostructures

Wei Pan, Jon F. Ihlefeld, Ping Lu, and Stephen R. Lee

Prepared by
Sandia National Laboratories
Albuquerque, New Mexico 87185 and Livermore, California 94550

Sandia National Laboratories is a multimission laboratory managed and operated by National Technology and Engineering Solutions of Sandia, LLC, a wholly owned subsidiary of Honeywell International, Inc., for the U.S. Department of Energy's National Nuclear Security Administration under contract DE-NA0003525.

Issued by Sandia National Laboratories, operated for the United States Department of Energy by National Technology and Engineering Solutions of Sandia, LLC.

Available to DOE and DOE contractors from

U.S. Department of Energy
Office of Scientific and Technical Information
P.O. Box 62
Oak Ridge, TN 37831

Telephone: (865) 576-8401
Facsimile: (865) 576-5728
E-Mail: reports@osti.gov
Online ordering: http://www.osti.gov/scitech

Available to the public from

U.S. Department of Commerce
National Technical Information Service
5301 Shawnee Rd
Alexandria, VA 22312

Telephone: (800) 553-6847
Facsimile: (703) 605-6900
E-Mail: orders@ntis.gov
Online order: https://classic.ntis.gov/help/order-methods/

SAND2017-
1107611076110761107611076110761107611076110761107611076110761107611076110
7611076110761107611076110761107611076110761107611076110761107611076110761
1076110761107611076110761107611076110761107611076110761107611076110761107
6110761107611076110761107611076110761107611076110761107611076110761107611
0761107611076110761107611076110761107611076110761107611076110761107611076
Printed October 2017
Unlimited Release

Emergent Phenomena in Oxide Nanostructures

Wei Pan
Quantum phenomena Department
MS 1086

Jon F. Ihlefeld
Electronic, Optical, and Nano
MS 1411

Ping Lu
Materials Characterization and Performance
MS 1411

Stephen R. Lee
Advanced Materials Sciences
MS 1086

Sandia National Laboratories
P. O. Box 5800
Albuquerque, New Mexico 87185-MS1086

Abstract

The field of oxide electronics has seen tremendous growth over two decades and oxide materials find wide-ranging applications in information storage, fuel cells, batteries, and more. Phase transitions, such as magnetic and metal-to-insulator transitions, are one of the most important phenomena in oxide nanostructures. Many novel devices utilizing these phase transitions have been proposed, ranging from ultrafast switches for logic applications to low power memory structures. Yet, despite this promise and many years of research, a complete understanding of phase transitions in oxide nanostructures remains elusive.

In this LDRD, we report two important observations of phase transitions. We conducted a systematic study of these transitions. Moreover, emergent quantum phenomena due to the strong correlations and interactions among the charge, orbital, and spin degrees of freedom inherent in transition metal oxides were explored. In addition, a new, fast atomic-scale chemical imaging technique developed through the characterization of these oxides is presented.

ACKNOWLEDGMENTS

This work was performed, in part, at the Center for Integrated Nanotechnologies, an Office of Science User Facility operated for the U.S. Department of Energy (DOE) Office of Science by Los Alamos National Laboratory (Contract DE-AC52-06NA25396) and Sandia National Laboratories (Contract DE-NA-0003525). We thank Prof. Q.X. Jia at University at Buffalo, The State University of New York for providing the PLD oxide samples.

A portion of this work was performed at the National High Magnetic Field Laboratory, which is supported by National Science Foundation Cooperative Agreement No. DMR-1157490 and the State of Florida. We thank E.S. Choi and Y. Jiang for their help.

TABLE OF CONTENTS

FIGURES

Figure 3.1 Four-terminal resistance Rxx characterization of a VAN sample of ZnO:LSMO. (a) Temperature dependence of Rxx. Rxx decreases monotonically from room temperature to 4K. (b)

1. INTRODUCTION

The field of oxide electronics has seen tremendous growth over two decades and oxide materials find wide-ranging applications in information storage, fuel cells, batteries, quantum sensing, and more. In fact, the prospect of oxide electronics [1] has been compared to what took place for III-V semiconductors ~50 years ago, with potential for broader impact. In transition metal oxides, the strongly correlated d-electrons and interactions of spin, charge, orbit, and lattice degrees of freedom determine their physical properties. Figure 1.1 is a plot from a review article by Zubko *et al.* [2] It shows the rich phase diagram due to the complex interactions in transitional metal oxides.

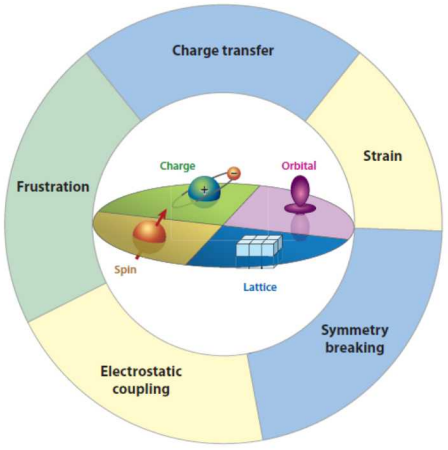

Figure 1.1 (adopted from Ref. [2]) complex physical behavior in transitional metal oxides due to strong interactions of charge, spin, orbital, and lattice degrees of freedom.

Phase transitions, such as magnetic transition and metal-to-insulator transition, are one of the most important phenomena in highly correlated oxide nanostructures. Many novel devices utilizing these phase transitions have been proposed, ranging from ultrafast switches for logic applications to low power memory structures. Yet, despite this promise and many years of research, a complete understanding of phase transitions in oxide nanostructures remains elusive.

We have studied emergent phenomena and novel phase transitions in transition metal oxide nanostructures that hold great promise for the next generation of electronics and functional devices. Results from this project will help to create a science-based knowledge foundation for creating, controlling, manipulating, and exploiting quantum particles in building 21st century technology. As a result of meeting structural characterization needs for these oxide materials, we have also developed a fast atomic-scale chemical imaging technique based on scanning transmission electron microscopy (STEM) using energy-dispersive x-ray spectroscopy (EDS).

In the following, we summarize the main results we have obtained in this project.

- ELECTRICAL CURRENT INDUCED MAGNETIC HYSTERESIS IN SELF-ASSEMBLED VERTICALLY-ALIGNED $La_{2/3}Sr_{1/3}MnO_3$:ZnO NANOPILLAR COMPOSITES

Magnetoresistive random-access memory (MRAM) is poised to become a next-generation information storage device. Yet, many materials challenges remain unsolved before it can become a widely used memory storage solution. Among them, is an urgent need to identify a material system that is suitable for downscaling and is

compatible with low-power logic applications. Self-assembled, vertically-aligned $La_{2/3}Sr_{1/3}MnO_3$:ZnO nanocomposites, in which $La_{2/3}Sr_{1/3}MnO_3$ (LSMO) matrix and

ZnO nanopillars form an intertwined structure with coincident-site-matched growth occurring between the LSMO and ZnO vertical interfaces, may offer new MRAM applications by combining their superior electric, magnetic (*B*), and optical properties. In this letter, we show the results of electrical current induced magnetic hysteresis in magneto-resistance measurements in these nano-pillar composites. We observe that when the current level is low, for example, 1 μA, the magneto-resistance displays a linear, negative, non-hysteretic *B* field dependence. Surprisingly, when a large current is used, $I > 10$ μA, a hysteretic behavior is observed when the *B* field is swept in the up and down directions. This hysteresis weakens as the sample temperature is increased. A possible spin-valve mechanism related to this electrical current induced magnetic hysteresis is proposed and discussed.

- CURRENT-INDUCED METAL-INSULATOR TRANSITIONS IN A SELF-ASSEMBLED VERTICALLY ALIGNED NANOCOMPOSITE THIN FILMS

Here, we present the first observation of a current-induced metal-insulator transition (MIT) in a ZnO:$La_{0.67}Sr_{0.33}MnO_3$ (ZnO:LSMO) VAN epitaxial film. The experimental results suggest that the diffusion of oxygen vacancies might be responsible for the observed MIT. We expect that the phenomenon discovered in this work can be further explored for nanoscale-switch applications.

- FAST ATOMIC-SCALE CHEMICAL IMAGING OF CRYSTALLINE MATERIALS AND DYNAMIC PHASE TRANSFORMATIONS

Atomic-scale phenomena fundamentally influence materials form and function, which makes the ability to locally probe and study these processes critical to advancing our understanding and development of materials. Atomic-scale chemical imaging by scanning transmission electron microscopy (STEM) using energy-dispersive x-ray spectroscopy (EDS) is a powerful approach to investigate solid crystal structures. Inefficient x-ray emission and collection, however, require long acquisition times (typically hundreds of seconds), making the technique incompatible with electron-beam sensitive materials and study of dynamic material phenomena. Here we describe an atomic-scale STEM-EDS chemical imaging technique that decreases the acquisition time to as little as one second, a reduction of more than 100 times. We demonstrate this new approach using $LaAlO_3$ single crystal and study dynamic phase transformation in beam-sensitive $Li[Li_{0.2}Ni_{0.2}Mn_{0.6}]O_2$ (LNMO) lithium ion battery cathode material. By capturing a series of time-lapsed chemical maps, we show for the first time clear atomic-scale evidence of preferred Ni-mobility in LNMO transformation, revealing new kinetic mechanisms. These examples highlight the potential of this approach toward temporal, atomic-scale mapping of crystal structure and chemistry for investigating dynamic material phenomena.

2. ELECTRICAL CURRENT INDUCED MAGNETIC HYSTERESIS IN SELF-ASSEMBLED VERTICALLY-ALIGNED $La_{2/3}Sr_{1/3}MnO_3$:ZnO NANOPILLARS COMPOSITES

2.1. Abstract

Magnetoresistive random-access memory (MRAM) is poised to become a next-generation information storage device. Yet, many materials challenges remain unsolved before it can become a widely used memory storage solution. Among them, an urgent need is to identify a material system that is suitable for downscaling and is compatible with low-power logic applications. Self-assembled, vertically-aligned $La_{2/3}Sr_{1/3}MnO_3$:ZnO nanocomposites, in which $La_{2/3}Sr_{1/3}MnO_3$ (LSMO) matrix and ZnO nanopillars form an intertwined structure with coincident-site-matched growth occurring between the LSMO and ZnO vertical interfaces, may offer new MRAM applications by combining their superior electric, magnetic (*B*), and optical properties. In this letter, we show the results of electrical current induced magnetic hysteresis in magneto-resistance measurements in these nano-pillar composites. We observe that when the current level is low, for example, 1 μA, the magneto-resistance displays a linear, negative, non-hysteretic *B* field dependence. Surprisingly, when a large current is used, $I > 10$ μA, a hysteretic behavior is observed when the *B* field is swept in the up and down directions. This hysteresis weakens as the sample temperature is increased. A possible spin-valve mechanism related to this electrical current induced magnetic hysteresis is proposed and discussed.

2.2. Introduction

Magnetoresistive random access memory (MRAM)[1,2] utilizes the change of electrical resistance in a magnetic (B) field to write, read, and store information. It has emerged as a promising candidate to replace conventional semiconductor memory structures, such as static RAM, dynamic RAM and flash memory, which are facing significant challenges of scaling capability as the semiconductor chip industry moves to smaller nodes. Indeed, as the size of these conventional memory structures is decreased, for example, down to 20 nm, leakage current presents a power consumption issue. MRAM, being nonvolatile in nature, has the potential to reduce power consumption drastically. At present, the size of MRAM bit cells is larger than that of conventional semiconductor memory devices. Consequently, a large driving current is required to change the associated magnetic states, thus presenting a power consumption issue. Therefore, one of the pressing needs is to identify new MRAM materials that are suitable for nanoscale device implementations and are compatible with low-power logic applications.

In this part, we explore the current induced magnetic properties of heteroepitaxial $(La_{2/3}Sr_{1/3}MnO_3)_{0.5}$:$(ZnO)_{0.5}$ (LSMO:ZnO) nanocomposites.[3] The phenomena observed from our experiments have suggested the potential application of such nanocomposites for MRAMs. These materials are grown using both pulsed-laser deposition (PLD) and rf magnetron sputtering, structurally characterized using

aberration-corrected scanning-transmission electron microscopy (AC-STEM) and x-ray diffraction (XRD), and electronically studied using low-temperature magneto-transport measurements. AC-STEM of the heteroepitaxial nanocomposite films reveals self-assembled, vertically-aligned ZnO nanopillar arrays featuring previously unreported nanometer-scale compositional redistribution around ZnO nanopillars; moreover, transport measurements demonstrate an electrical current induced magnetic-hysteretic behavior of the nanocomposite. The small nanopillar size, together with this observation of novel current induced magnetic-hysteretic behavior, makes this material system a potentially ideal platform for next-generation MRAM applications.

2.3. Results and Discussions

Fig. 2.1 left panel shows a schematic diagram of a self-assembled epitaxial nanocomposite thin film, where LSMO matrix and ZnO nanopillars form an intertwined structure with coincident-site-matched or domain-matched growth[4] occurring between the LSMO and ZnO vertical interfaces.[5] Fig. 2.1 middle panel shows a cross sectional STEM high-angle annular dark field (HAADF) image of such a sample. The thickness of the epilayer is about 50 nm. It is clearly seen that vertically aligned epitaxial nanocomposite film is achieved on the 001_p-oriented $LaAlO_3$ (LAO) substrate (where the *p* denotes pseudocubic indices), consistent with the schematic drawing shown in Fig. 2.1 left panel. The average width of the nanopillars (ZnO) is around 10 nm. Fig. 2.1 right panel shows a reciprocal space mapping XRD pattern of the (002) reflection of the LSMO:ZnO nanocomposite film. The horizontally broadened LSMO peak shape along Q_x in Fig. 2.1 right panel reflects the presence of both misfit dislocations and the quasi-periodic pillar structures in the composite epilayer, as both phenomena alter the lateral coherence of the epilayer's crystal structure. Additional {103} and {113} reciprocal space maps (not shown) find that the LSMO lattice-mismatch strain at the growth interface to the LAO substrate is ~80% relaxed.

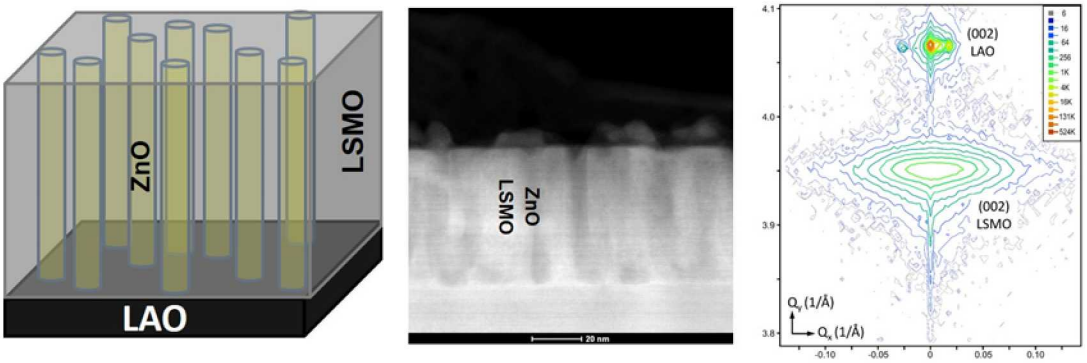

Figure 2.1 Left: a schematic diagram of a self-assembled epitaxial nanocomposite thin film. Middle: a cross sectional STEM high-angle annular dark field (HAADF) image of such a sample. Right: a reciprocal space mapping XRD pattern of the (002) reflection of the LSMO:ZnO nanocomposite film.

Further XRD measurements of the $(10\bar{1}0)$ and $(11\bar{2}0)$ reflections of the ZnO find the same epitaxial orientation of the ZnO relative to the LSMO and LAO as previously reported by Chen *et al*. for similar growths on STO substrates,[5] where a $[11\bar{2}0]$ direction of the ZnO lies normal to the sample surface and [0001] of ZnO lies parallel to the surface and along <110> directions of the LSMO/LAO. As discussed by Chen *et al*., this orientation gives rise to an approximate coincident-site-type or domain-type lattice matching of the composite heterolayer and the substrate.[4] The nanostructure and strain of the composite is particularly influenced by a close domain matching of the LSMO and ZnO along the surface normal, where the height of five (002) LSMO planes (5 × 1.9425 = 9.713 angstroms) matches to an adjacent stacking of six $(11\bar{2}0)$ ZnO planes (6 × 1.6249 = 9.749 angstroms). The resulting domain-size matching at the nanopillar- sidewall interfaces is within ~ 0.4%, hence the preferred $(11\bar{2}0)$ ZnO orientation.

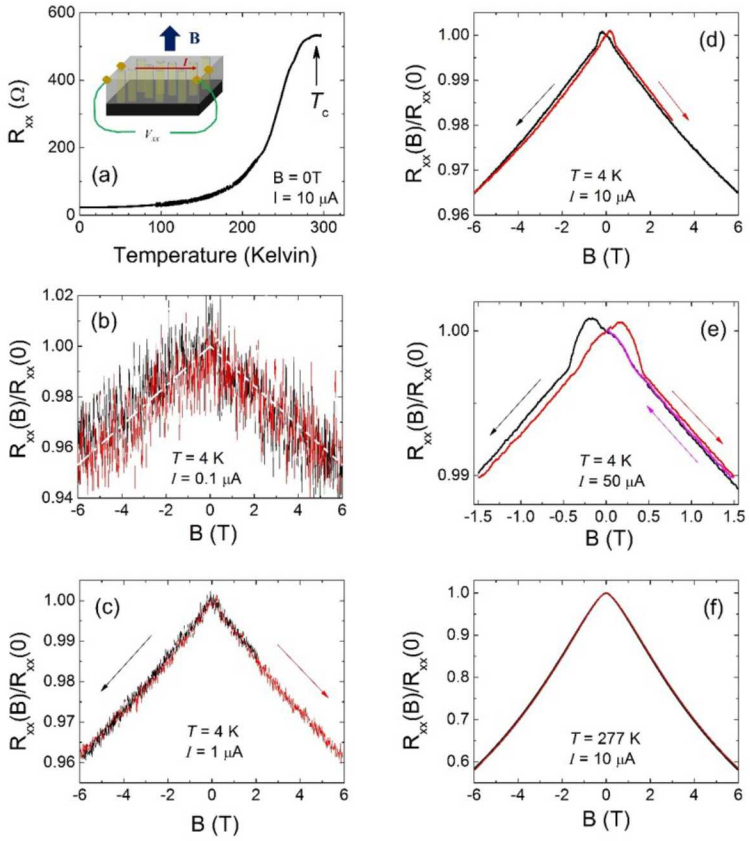

Figure 2.2 (a) Magnetoresistance (R_{xx}) as a function of temperature (T) at zero B field. (b)-(e) R_{xx} as a function of B field, with each panel showing a different combination of excitation current at a fixed measurement temperature of T = 4 K. (f) R_{xx} as a function of B field at a fixed measurement temperature of T = 277 K. The current is 10 μA.

In Fig. 2.2a, we show the magnetoresistance (R_{xx}) as a function of temperature (T) at zero B field in a LSMO:ZnO nanocomposite with a film thickness of 200 nm. The

inset of Fig. 2.2a shows the schematic drawing of measurement configuration. As the temperature falls from 290 K to 1.4 K, R_{xx} also decreases continuously, indicating a metallic behavior. A broad peak is observed to be forming near $T \sim 290$ K, indicating the onset of a metal-insulator transition. The observed critical temperature, $T_c \sim 290$ K, is similar to the value reported in a previous study.[5] Also consistent with previous work, a stronger magneto-resistance is observed at high temperatures close to T_c.[6] Note here the B field is measured in units of Tesla (T). As shown in Fig. 2.2c and Fig. 2.2f, the measured normalized magnetoresistance (MR) at $B = 1$ T (defined as MR = $(R_{xx}(0)-R_{xx}(B))/R_{xx}(0)$) is ~ 7% at $T = 277$K, compared to ~ 0.7% at 4 K.

The main results of this letter are shown in Figs. 2.2b-2.2e where R_{xx} is plotted as a function of B field, with each panel showing a different combination of excitation current at a fixed measurement temperature of $T = 4$ K. When a small excitation current of 0.1 μA is used (Fig. 2.2b), R_{xx} displays a negative, linear B field dependence. We note here that the trace is quite noisy, exceeding the resolution of our measurements. Possible physical origins for this excess noise are under investigation. R_{xx} is measured for the B field sweeping from -6 to 6 T (red) and then from 6 to -6 T (black). The two curves show good overlap given the noisiness of the low-current measurements. As the current is increased to 1 μA at fixed T (Fig. 2.2c), the noise level becomes much smaller and the linear B field dependence also becomes much clearer. Still, there is no well-defined hysteresis for the B field as it sweeps up and down.

Notably, the magnetic field dependence changes dramatically when the excitation current is increased to 10 μA at fixed T (Fig. 2.2d). Here, a pronounced hysteretic behavior is observed for the B as it sweeps up and down. Indeed, as the B field is swept downward from an initial value of 6 T, R_{xx} increases linearly with the decreasing B field until it reaches a maximal value at $B \sim -0.2$ T. Just below this field, R_{xx} drops relatively sharply for a small segment of the sweep and then abruptly transitions back to a linear regime where R_{xx} now decreases with increasingly negative B. Upon reversing the sweep and coming back from -6 T, R_{xx} first increases linearly with the decreasingly negative B field, but in this reverse sweep, the field reaches its maximal value at $B \sim +0.2$ T. Finally, just above this field, there is again a relatively sharp drop and then a repeated transition back to a linear regime, where now R_{xx} decreases linearly with increasing B. These two overlapping-sweep traces clearly show a "butterfly-shaped" hysteretic behavior, where the magnetoresistance centers at about zero field. The hysteretic behavior becomes stronger as higher currents are used (e.g. 50 μA Fig. 2.2e).

Examining Fig. 2.2e carefully, we also notice that a very weak local minimum seems to be developing at $B = 0$ T. Indeed, as shown later in Fig. 4a, a double-peak structure (one weak and one strong) is developed around $B = 0$ T and ΔR_{xx} approaches zero after the linear background is subtracted. Moreover, Fig. 2.2e shows that there is no drift in the resistance states. Indeed, after the B field is swept from – 1.5 T to 1.5 T, the B field sweeping direction is reversed immediately and swept back to zero for a second time

(unlike in Figs. 2.2b-2.2d). The second down-sweeping curve (blue) overlaps exactly with the initial downward-sweeping-B curve (black) from 3 T to 0 T. The hysteretic behavior completely disappears at elevated temperatures. In Fig. 2.2f, we show an R_{xx} curve taken at 277 K, close to T_c, where the excitation current is in a high-current regime, 10 μA. Unlike the low-temperature high-current measurements, the magnetoresistance curves for the two B sweeping directions now exactly overlap with each other.

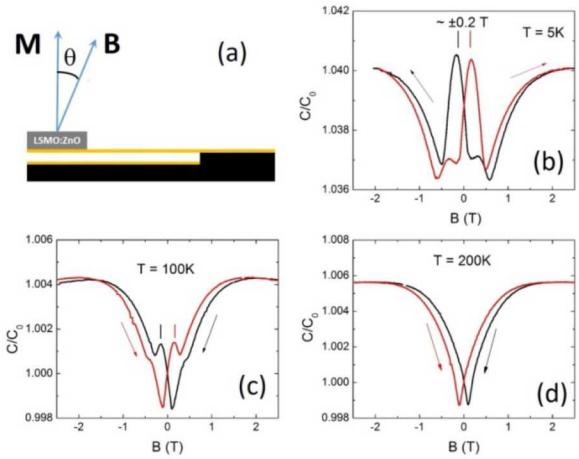

Figure 2.3 magnetic torque results at various temperatures.

Next, we present results from magnetic torque measurements, which show that the observed hysteretic behavior is most likely related to the magnetization (M) of the specimen. In Fig. 2.3a, a schematic diagram of the capacitive cantilever for magnetic torque measurement is shown in which B is applied at a tilt angle of θ to the sample normal, and a magnetic torque $\tau = M \times B$ is generated and deflects the cantilever. This deflection is detected by measuring the capacitance (C) between the cantilevered metal plate (the top golden rectangle shown schematically in Fig. 2.3a) where the sample sits and the fixed metal plate (the bottom golden rectangle in Fig. 2.3a).[7] As long as the change of the capacitance is small (in our case, less than 1%), the torque is proportional to the measured capacitance minus the zero-field balanced capacitor value C_0 (~ 1 pF for our sample).[7] Consequently, the magnetization can be deduced. Fig. 2.3b shows the normalized capacitance value (C/C_0) as a function of the magnetic field for magnetometry performed at low temperature (T = 5 K). θ is about 11 degrees. The B field is first swept from 2.5 to -2.5 T. At higher $|B|$ fields, C/C_0 shows weak B field dependence. As B is decreased, C/C_0 decreases and then displays a weak local maximum at $B \sim +0.3$ T. A larger peak is observed at $B \sim -0.2$ T. Sweeping the B field from -2.5 to 2.5 T, a weak peak is observed at $B \sim -0.3$ T and a larger peak at $B \sim +0.2$ T. We point out that the positions of the large peaks are the same as the B field positions where the resistance maxima occur in Figs. 2.2d and 2.2e when the B field is swept along the same direction. The coincidence can be seen more clearly in Fig. 4 by comparing C/C_0 and ΔR_{xx} of I = 50 μA. Here, ΔR_{xx} is obtained after subtracting the

linear background. This strongly suggests that the hysteretic resistance behavior is related to the magnetization of the specimen. Finally, the B field positions (~ ± 0.3 T) of the weaker peaks in C/C_0 correspond well with the abrupt up-kinks in the magneto-resistance also seen in Fig. 2.2, and the dips around B = 0 T in C/C_0 seem to correspond well to the weak peaks in ΔR_{xx}.

Elevated-temperature magnetic torque measurements were also carried out. Fig. 2.3c shows results for T = 100 K. At this temperature, the peaks at B ~ ± 0.2 T become much weaker. After the temperature is raised to T = 200 K (Fig. 2.3d), the peaks at B ~ ± 0.2 T are all but gone, which is consistent with the 277 K disappearance of the magnetoresistance hysteresis seen in Fig. 2.2f.

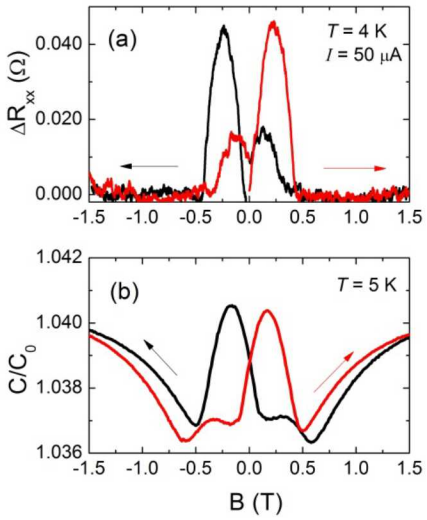

Figure 2.4 Comparison of magnetoresistance and magnetic torque measurements.

The B field dependence of our magneto-transport data suggests that there are two contributions to the magnetoresistance. At higher magnetic field, the intrinsic negative linear magnetoresistance is most likely due to the suppression of spin fluctuations, as observed in Ref. 8. At a lower magnetic field of around B = 0, the magnetoresistance appears to be due to a tunneling process, which is only active at higher electric field (or higher electrical current). In the following, we will discuss two possible mechanisms that may be responsible for the observed electrical current induced magnetization behavior.[9] First, we note that the "butterfly" shape of the magnetoresistance hysteresis is very similar to that in a spin valve device,[10,11] where the hysteresis is due to the switching of magnetization in the so-called free layer. Based on this similarity, it is natural to speculate that the same spin valve mechanism is also responsible for the hysteresis observed in our experiment.

Our high-resolution STEM analysis supports this hypothesis. In Fig. 2.5a, we show the STEM-HAADF image in plan-view of an LSMO:ZnO nanopillar composite grown by

magnetron sputtering method (details of growth is given in the method section). A transition region is visible around ZnO in this HAADF image. To further examine this transition region, STEM energy-dispersive x-ray spectroscopy (EDS) mapping was carried out for the sample. Fig. 2.5b shows a composite color EDS map, made of zinc *K* (red), strontium *K* (blue)), lanthanum *L* (green), and manganese *K* (cyan) maps. The individual map for each element is also shown in Fig. 2.5c. A core-shell structure around the ZnO nanopillars, corresponding to a (La, Mn)-rich and Sr-deficient region, is clearly visible in Fig. 2.5b. This is very unique for such a nanocomposite architecture.

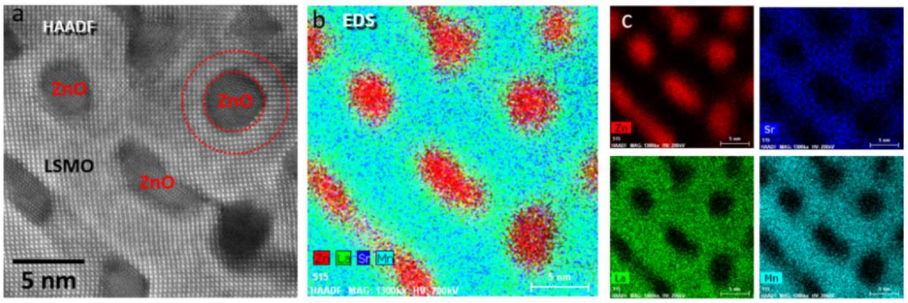

Figure 2.5 STEM-HAADF image in plan-view of an LSMO:ZnO nanopillar composite grown by magnetron sputtering method.

Due to this Sr-deficiency, it can be expected that the shell layer may possess a different magnetization, compared to the nominal, stoichiometric $La_{2/3}Sr_{1/3}MnO_3$ composition. When a low current is used, this Sr-deficient shell layer maintains a ferromagnetic ground state as in $La_{2/3}Sr_{1/3}MnO_3$. Consequently, no magnetization switching, and thus hysteresis, is expected. The resulting low-current electronic transport is likely due to spin polarized electron tunneling between the LSMO and the Sr-poor LSMO domains, which leads to a linear *B* field dependence, as was previously observed in Ref. 8 for structurally analogous intergrain transport for polycrystalline LSMO. On the other hand, a high electric field (or a high electrical current) can modify the magnetic anisotropy and thus alter the direction of magnetization,[12-14] and an electric field (or electrical current) induced transition from ferromagnetic to antiferromagnetic ground states may occur.[13] In this regard, it is possible that at higher electrical currents in our experiments, the magnetization of the Sr-deficient shell layer is tilted from (or in the extreme limit antiparallel to) that of LSMO. In this configuration, a spin valve behavior is expected and this can give rise to the observed *B* field induced resistance hysteretic behavior.

An alternative possibility is related to the possible magnetization of the ZnO nanopillars themselves, not the Sr-poor layer. It is known that a small amount of background carbon may incorporate into the film during the composite-film growth.[3] As a result, the ZnO nanopillars may become weakly ferromagnetic.[15] As already noted above, a high electric field (or electrical current) can vary the direction of *M*.[12-14]

In this alternative scenario, it is possible that at a low electrical current the *M* in ZnO is aligned with the *M* in LSMO, and electronic transport is again dominated by spin polarized electron tunneling, but now between the LSMO and ZnO nanopillars (instead of the between the LSMO and the Sr-poor LSMO domains as described above), and a negative linear *B* field dependence is again expected.[8] At a high electrical current, the *M* in ZnO may lie in the plane, and as the amplitude of $|B|$ field increases, *M* eventually switches its direction and becomes parallel to the *M* in LSMO. This switching behavior of the *M*, now occurring in the ZnO, can again give rise to a butterfly shaped magnetoresistance hysteresis, as observed.

2.4. Further Remarks

A few remarks are in order. First, we note that the current density to induce the magnetic hysteresis is quite low in our sample. The cross-sectional area of the contact is about 200 nm × 1 mm, and at the observed critical current between approximately 1 and 10 μA, the critical current density becomes only ~ 5×10^3- 5×10^4 A/m^2, significantly lower than ~ 10^6 A/m^2 in a typical MRAM device.[9] This small current density may find unique applications in low-power memory devices. Second, we point out that the electrical-current-induced magnetic hysteresis is observed in a planar device structure, different from a sandwich device structure in a MRAM memory cell. This can help to increase magnetic memory cell density, and also make the cell fabrication much easier. Third, among the many available composite heterostructures formed using LSMO,[3] the LSMO:ZnO composite forms one of the most promising self-organized structures. This promise arises in part from the ability to tune the heteroepitaxial strain state, the compositional distribution, the nanostructure, and the resultant magneto-electronic properties of the LSMO:ZnO composite. As shown in previous work,[3] the tunability of strain and structure specifically arises through the introduction of differing composite-layer stoichiometries and the use of differing substrates (LAO, STO, and others). As we have shown here, the attendant variations in structure directly alter the magneto-electronic properties. Beyond these nanostructural effects, $La_{2/3}Sr_{1/3}MnO_3$ is a *p*-type, metallic ferromagnet, whose magnetic properties can be readily tuned by dopant-induced control of the carrier concentration. We also note that ZnO is an *n*-type large band-gap semiconductor; it is earth abundant and non-toxic; and its electrical properties can be tuned by opto-electrical means. Thus, in heteroepitaxially fabricated LSMO:ZnO *p-n* junctions, one should be able to control and manipulate the electrical and magnetic properties by a variety of magneto-opto-electrical means.

Such devices may ultimately enable a new generation of opto-magneto MRAM applications. Of course, all the measurements reported in this manuscript were carried out at cryogenic temperatures, and thus, LSMO:ZnO composites remain impractical for immediate, real-world applications. Nonetheless, as these promising materials and their physics become more thoroughly explored, understood, and optimized, one may be able to realize the electrical current induced magnetic hysteresis at substantially higher temperatures, perhaps even room temperature.

3. CURRENT-INDUCED METAL-INSULATOR TRANSITIONS IN A SELF-ASSEMBLED VERTICALLY ALIGNED NANOCOMPOSITE THIN FILMS

Self-assembled vertically aligned nanocomposite (VAN) epitaxial films [1] have attracted a great deal of current interest. In these nanocomposite films, large interface areas produced by the reduced dimensionality play an important role in determining the structural and functional properties [2,3]. Moreover, the coupling of different functionalities in the highly dissimilar components of such films provides a vast parameter space for exploiting interface properties and functionalities. This feature makes VAN films an exceptional platform that provides new opportunities for improved multi-functionalities that are not available from bulk crystals. In this Letter, we present the first observation of a current-induced metal-insulator transition (MIT) in a ZnO:$La_{0.67}Sr_{0.33}MnO_3$ (ZnO:LSMO) VAN epitaxial film. The experimental results suggest that the diffusion of oxygen vacancies might be responsible for the observed MIT. We expect that the phenomenon discovered in this work can be further explored for nanoscale-switch applications.

Among many exotic transport properties in perovskite magneto-resistive manganites [4], the metal-insulator transition (MIT) [5-8] remains as one of the most fascinating phenomena exhibited by these materials. The MIT is not only intrinsically linked to the strong coupling of orbit, spin, and charge in the perovskite rare-earth manganites but also can be used in exciting applications, such as ultrafast electrical switches, nonvolatile memory devices, etc [8,9]. While studies of the MIT have mainly been carried out in bulk manganites, the less-studied nanostructured manganites may prove especially interesting because of the inherently large interface area often present in nanostructured materials. This extensive interface structure may cause the MIT phenomena to manifest a totally different way.

To investigate this possibility, we have studied self-assembled VAN epitaxial thin films of ZnO:LSMO grown on (001) $LaAlO_3$ (LAO) substrates, as shown schematically in Fig. 2.1 left panel. While recent composite films of ZnO:LMSO have been grown by using either pulsed laser deposition (PLD) or rf magnetron sputtering [10-14], this paper will focus on a PLD-grown thin film. The composite film of 200 nm thickness was deposited using a KrF excimer laser (λ = 248 nm). The substrate temperature and oxygen pressure during the deposition were maintained at 750 °C and 300 mTorr, respectively. These processing parameters have routinely been used to prepare high-crystallinity LSMO and ZnO:LSMO films in previous work using PLD [10,11]. Figure 2.1 middle panel shows a high-resolution cross sectional TEM [15] image for this sample. It is clearly seen that composite ZnO:LSMO nanopillar arrays are achieved on the LAO substrate. The average width of the pillars is around 10 nm. The well-defined diffraction spots can be indexed as (002) LSMO and (110) ZnO. Figure 2.1 right panel shows an x-ray diffraction (XRD) reciprocal-space map of the

ZnO:LSMO film. The relatively broad lateral peak width of the (002) quasicubic reflection of the LSMO (seen also in a (103) and (113) asymmetric maps, not shown here) reflects the combined presence of both misfit dislocations and the quasi-periodic nano-columnar character of the LSMO epilayer. As seen in the TEM, columnar ZnO domains segregate within the LSMO, but do not appear in the XRD because of the highly dissimilar crystal structure and orientation of the ZnO. In addition, the LAO substrate shows multiple weaker peaks lateral to the main peak, indicating the presence of substrate domain boundaries produced by stacking faults in the bulk LAO. From the XRD data, we determine that the out-of-plane lattice parameter of LSMO is ~ 3.905Å, slightly elongated in comparison with its bulk form (~3.870 Å). This is not unreasonable considering the substantial, but significantly relaxed, lattice-mismatch strains exerted on the LSMO pillars by both the LAO substrate and the interspersed ZnO.

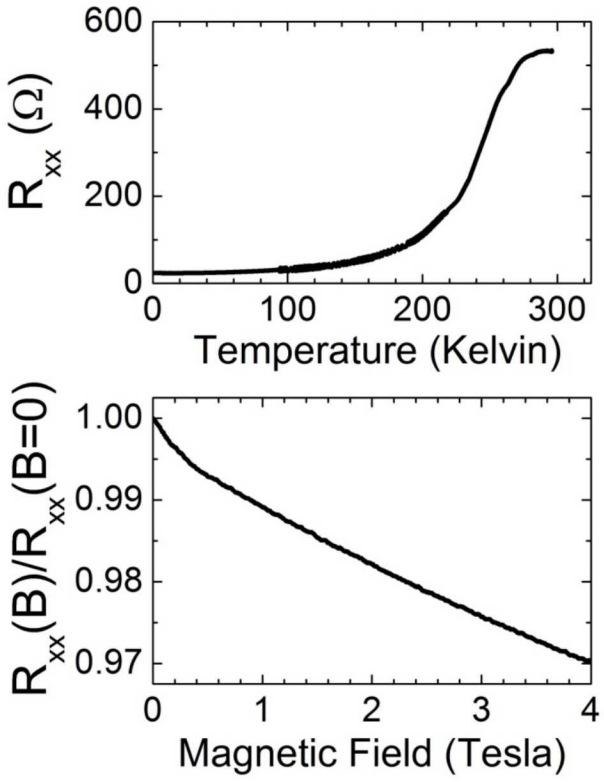

Figure 3.1 Four-terminal resistance R_{xx} characterization of a VAN sample of ZnO:LSMO. (a) Temperature dependence of R_{xx}. R_{xx} decreases from room temperature to 4K. (b) Magneto-resistance taken at 4K. A linear magnetic field dependence is observed in high magnetic fields.

In Fig. 3.1 we show results from the measurements of four-terminal longitudinal resistance R_{xx}. Figure 3.1(a) shows the temperature (T) dependence of R_{xx} at zero magnetic field. It decreases continuously from ~ 520 ohms at 300 K to ~ 23 ohms at 0.3 K. No paramagnetic to ferromagnetic transition is seen in this temperature range. This is consistent with a previous report, where a ZnO:LSMO VAN thin film of 350

nm thickness exhibited a transition temperature at 330 K [1]. This result is also not much different from that in a pure LSMO thin film of 280 nm thickness (~350 K). Figure 3.1 (b) shows the normalized magneto-resistance (MR) taken at $T = 4$ K, with the magnetic field (B) applied along the current direction. The MR initially decreases parabolically by ~ 0.5% as B increases from 0 to 0.5 T; it then transitions to a linear dependence on magnetic field and experiences another 2.5% decrease from 0.5 to 4 T. Similar magneto-transport features have been observed in other VAN samples [16]. The relatively fast drop in the low-field regime might be due to spin-polarized tunneling between magnetic domains [17]. Compared to the MR in previous polycrystalline samples [17], the low-field drop in the VAN film is less steep, indicating a better crystallinity of LSMO in our sample.

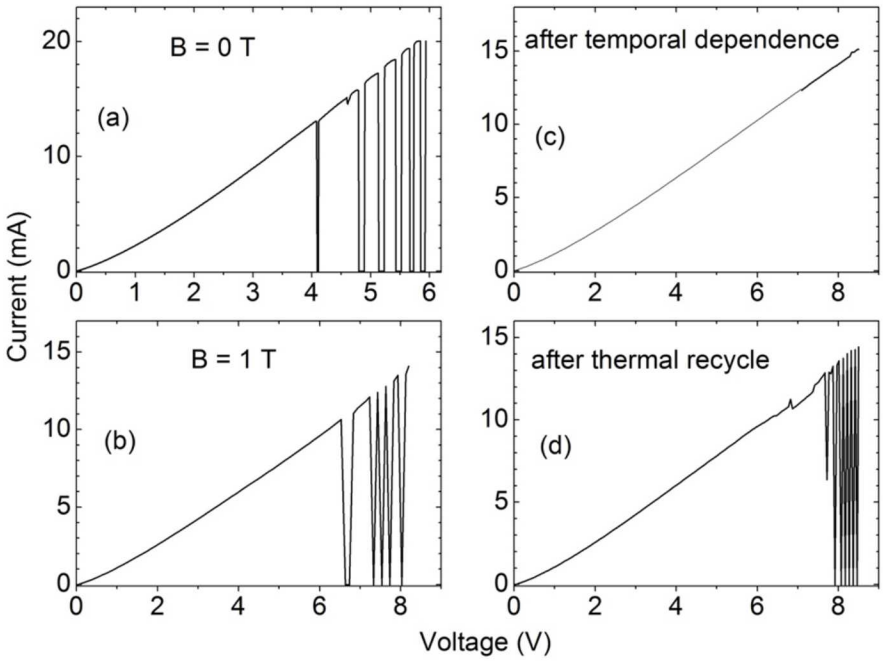

Figure 3.2: Current-voltage curves taken at 4 K at various experimental stages. (a) I-V measurement when the sample was fist cooled down. The current-induced metal-insulator transition (MIT) events are observed. (b) I-V at a non-zero magnetic field of 1 Tesla in the same cool down. The same current-induced MIT events are seen. (c) I-V curve measured right after the temporal dependence in Fig. 3.3(a). No current-induced MIT events are visible. (d) I-V curve after thermal recycle of sample. The current-induced MIT events reappear.

In the following, we will focus on our surprising observation of a current-induced metal-insulator transition (MIT), obtained through extensive use of current-voltage (I-V) measurements. Figure 3.2(a) shows an I-V curve taken at 4 K, where overall, the I-V curve is linear. Surprisingly, when the direct current bias (V_{DC}) is larger than 4 V and the current exceeds 10 mA, a MIT is observed where at some random V_{DC}, the current (I), or the conductance (defined as I/V_{DC}), of the sample suddenly drops to zero. This zero-conductance state dwells for a few seconds before the current rises

sharply and re-assumes a value more or less determined by linear extrapolation of initial low-bias regime. With continued increases in V_{DC}, this current-induced MIT event intermittently repeats itself in a similar fashion. Figure 3.2(b) shows a similar I-V curve measured at B = 1 T, and again, the current induced MIT was observed. Thus, the same MIT behavior was observed at both zero and finite magnetic fields.

To further understand this current-induced MIT phenomena, we carried out a temporal study wherein V_{DC} was fixed at 7.1 V, the magnetic field was reset to zero, and the current was recorded as a function of time, yielding the results shown in Fig. 3.3(a). It is striking to observe that the current switches randomly between ~ 12 and 0 mA. The dwell time of the zero conductance states varies from 3 to 13 seconds. Eventually, the current-induced MIT events disappear, and the current stays more or less constant with time. In Fig. 3.3(b), we plot histogram of the dwell time of each zero-conductance-state event. It can be seen that the zero-conductance states persist for an average time of ~ 6.5 seconds.

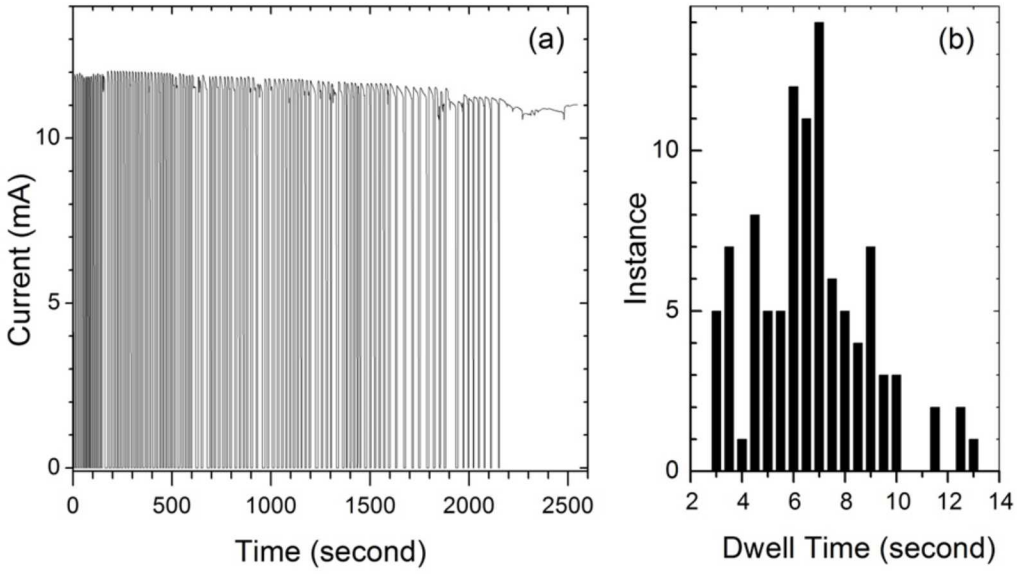

Figure 3.3 Temporal dependence of the current-induced metal-insulator transition (MIT). (a) The DC bias was set at V_{DC} = 7.1 V. The recorded current is plotted as a function of time. (b) Histogram of data presented in panel (a) where the instance of each zero conductance state is plotted in binned fashion as a function of the dwell time of the state.

Immediately after the disappearance of the current-induced MIT seen in Fig. 3.3, we re-examined the behavior of the I-V curve and found that the I-V curve only shows the linear dependence, as seen in Fig. 3.2(c). Next, we thermally cycled the sample to room temperature and then cooled it back to 4 K, where I-V measurements were again

repeated. After thermal cycling, the current-induced MIT was observed to return, as shown in Fig. 3.2(d).

We point out here that this current-induced switching between a zero-conductance state and a conducting state, as well as its quasi-periodic characteristic timing behavior, differs drastically from the current switching of resistive states seen in another manganite, $(Pr,Ca)MnO_3$ [6], where a hysteric switching event was observed. On the other hand, the switching behavior observed in our VAN thin film resembles somewhat the resistive switching seen at the Ag-$Pr_{0.7}Ca_{0.3}MnO_3$ interface reported in Ref. [7]. Motivated by the arguments for an electrochemical migration model suggested in Ref. [7], we will discuss below two possible origins for the current-induced MIT seen in our sample.

First, based on the observation of the disappearance of the current induced MIT events in the temporal dependence study of Fig. 3.3, one may conclude that an electrochemical change arises in our specimen as a result of protracted current exposure at fixed bias . One candidate process to consider is the diffusion of positively charged oxygen vacancies. It is known that an as-grown LSMO film contains many oxygen vacancies and they are mobile. Under a large voltage bias, these oxygen vacancies can move and accumulate at the interface between LSMO and ZnO, where the impedance is large. This large impedance, together with a large DC current, generates a highly localized joule heating that dramatically increases the local temperature. This, in turn, might drive the interface areas and, eventually, the whole sample insulating, thus giving rise to a metal-insulator transition. As the whole sample becomes insulating, the current flow through the sample almost ceases causing the joule heating to stop. As a result, the local temperature at the interfaces is reduced and the sample becomes metallic again. Consequently, the current can resume flow and assume the value determined by the original, linear, ohmic law behavior. With a continuous increase of current, the current-induced metal-insulator transition then repeats. Eventually, when the oxygen-vacancy diffusion process completes and stops, the MIT events disappear, as we see in Fig. 3.3(a). We emphasize here that the large area of interface between LSMO and ZnO is crucial for the observed current-induced MIT events. In fact, in a reference sample of pure LSMO grown epitaxially on LAO under the same growth conditions to the same thickness, no current-induced MIT events were observed.

Though the above model captures most of the transport behaviors we observed in our experiment, the most distinctive feature in our measurements -- a complete zero-conductance state -- was not explained. Moreover, as shown in Fig. 3.2(a), the R_{xx} value is still relatively low, ~ 500 ohms at 300 K. At this value of resistance, the sample is quite conductive, and a complete zero-conductance state should not be expected.

Thus we considered a second model that also involves oxygen vacancies. It is known that the formation energy of oxygen vacancies is typically smaller at the surface compared to the bulk [18]. As a result, it has been predicted that approximately 10^6 times higher vacancy concentrations exist at or near the surface compared to in the bulk in $La_{0.9}Sr_{0.1}MnO_3$ [18]. We might expect a similar effect in our VAN specimen with, perhaps, the ensemble of ZnO and LSMO domains and interfaces interacting to further enhance oxygen-vacancy formation. Now, under a large bias voltage, the injected negative electrons can make the surface areas underneath the contact electrodes neutral by combining with positively charged population of oxygen vacancies arising in the VAN structure. This, in turn, can be expected to induce a metal-insulator transition and, consequently, the zero-conductance state. Within the zero-conductance state, surface oxygen vacancies outside the contact electrode areas will move towards the contacts, making these areas positively charged again and, thus, terminating the zero-conductance state. It can be imagined that this current-induced MIT event will repeat itself until all the oxygen vacancies are neutralized.

FAST ATOMIC-SCALE CHEMICAL IMAGING OF CRYSTALLINE MATERIALS AND DYNAMIC PHASE TRANSFORMATIONS

3.1. Abstract

Atomic-scale phenomena fundamentally influence materials form and function, which makes the ability to locally probe and study these processes critical to advancing our understanding and development of materials. Atomic-scale chemical imaging by scanning transmission electron microscopy (STEM) using energy-dispersive x-ray spectroscopy (EDS) is a powerful approach to investigate solid crystal structures. Inefficient x-ray emission and collection, however, require long acquisition times (typically hundreds of seconds), making the technique incompatible with electron-beam sensitive materials and study of dynamic material phenomena. Here we describe an atomic-scale STEM-EDS chemical imaging technique that decreases the acquisition time to as little as one second, a reduction of more than 100 times. We demonstrate this new approach using $LaAlO_3$ single crystal and study dynamic phase transformation in beam-sensitive $Li[Li_{0.2}Ni_{0.2}Mn_{0.6}]O_2$ (LNMO) lithium ion battery cathode material. By capturing a series of time-lapsed chemical maps, we show for the first time clear atomic-scale evidence of preferred Ni-mobility in LNMO transformation, revealing new kinetic mechanisms. These examples highlight the potential of this approach toward temporal, atomic-scale mapping of crystal structure and chemistry for investigating dynamic material phenomena

3.2. Introduction

Chemical imaging at the atomic-scale provides a useful real-space approach to investigate material structures and has been recently demonstrated in aberration corrected scanning transmission electron microscopy (STEM)[1-11]. By scanning an angstrom-sized electron probe across a crystal sample aligned along a low-axis orientation and collecting either electron energy-loss spectra (EELS)[1-4] or energy-dispersive x-ray spectra (EDS)[5-11], chemical imaging at atomic-scale has been achieved. Simultaneously recorded Z-contrast or high-angle annular dark-field (HAADF) images by using electrons that have been scattered over large angles and exited through the specimen are often used to provide reference images for atomic columns[1]. Since unique chemical signals are used for identification of the atomic columns in chemical imaging, determination of the lattice structures which might otherwise not be possible by traditional imaging or diffraction techniques (*e.g.*, electron, neutron, and x-ray diffraction) has also been demonstrated[10].

Arguably the greatest advantage of atomic-scale STEM EDS chemical imaging is that it allows for direct correlation between the atomic structure and the chemical map. Current methods, however, are limited by inefficient x-ray generation and collection. To compensate for this poor efficiency, STEM EDS datasets are often acquired as a series of frames, where the same region is typically scanned several hundred times, relying on spatial drift correction to build a high fidelity dataset[10-11]. This process usually takes more than a few hundred seconds, subjecting the samples to high doses

of electron irradiation. The requirement for extended acquisition times prevents the use of this technique for any electron beam sensitive materials and precludes the study of critical phase transformations and dynamics, which requires structural *and* chemical information resolved on a much shorter time scale. On the other hand, although time-resolved structural techniques (*e.g,* such as x-ray diffraction) are available, those techniques typically have inherent limitations on local structure and chemical determination and require relatively large samples[12].

Here we report the realization of rapid atomic-scale chemical imaging by STEM EDS from small crystalline region achieved with a total acquisition time of less than one or a few seconds under normal high-resolution STEM imaging conditions. Using $LaAlO_3$ as a model crystal, we find averaged atomic-scale chemical maps for lanthanum and aluminum atoms can be extracted from an area of ~ few 10 nm^2 acquired with the acquisition time of ~2 seconds or less. The method is verified by a phenomenological model. Furthermore, we apply the technique to study of the phase transformation in $Li[Li_{0.2}Ni_{0.2}Mn_{0.6}]O_2$ (LNMO), a lithium ion battery cathode material known to undergo an electron-beam induced phase transformation[13-15]. By obtaining atomic-scale structural information sequentially as a time series, it reveals for the first time that the transformation takes place by preferably jumping of nickel atoms (relative to manganese atoms) from the TM layers to the lithium layers once the lithium atoms are removed by the high-energy electrons. This capability opens up a new paradigm of study where chemical structure of materials susceptible to electron irradiation as well as phase transformation and dynamics can be followed temporally at the atomic-scale.

Our approach to overcome the limitation due to inefficient x-ray generation and collection is based on the following key considerations: (1) within the crystal area scanned (*e.g.*, 10×10 unit cells) for atomic-scale STEM EDS mapping, the seemingly random and sparsely scattered x-ray signals produced after a short acquisition time (*i.e.*, less than a few seconds) are not random but are statistically localized to atomic columns in the crystal; (2) the long range order of the crystal lattice creates chemically and structurally equivalent pixel positions within the scanned image, separated by precise lattice-vector translations; and (3) the x-ray counts, distributed over the large area, can be translated and summed across equivalent positions within one unit cell via lattice-vector translations, forming averaged chemical maps for the crystal. In the other words, the technique consolidates the x-rays scattered over a large area into a smaller, single unit cell area using lattice-vector translations, producing averaged chemical maps for the crystal. By concentrating x-ray signals into the smaller area, an acquisition time savings of over 100 times can be achieved. Localization of x-rays to atomic-columns is crucial to the successful outcome of the atomic-scale mapping and can be fulfilled by using a thin specimen and a small electron probe[8, 10-11]. Below we first demonstrate the technique on data obtained from a $LaAlO_3$ crystal.

3.3. Results and Discussions

$LaAlO_3$ has a perovskite crystal structure with a rhombohedral unit cell (a=0.3788 nm and α=90.4°). For practical considerations, it can be regarded as pseudo-cubic. Its

projected structure in the [001] direction is shown Fig. 4.1a. Figure 4.1b shows a raw EDS composite map (200×200 pixels) of La L (red-dot) and Al K (green-dot) x-rays, obtained after ~1.8 sec collection, corresponding to the sum of 3 frames (~0.6 sec per frame with an instantaneous dwell time on each pixel of 15 μsec). The spectral image was acquired for a physical frame size of 4.46 nm×4.46 nm (~0.022 nm/pixel). The reference HAADF image obtained simultaneously is shown in Fig. 4.1c (only ¼ of the image is shown). The multi-slice simulations[16] of the electron wave-function distribution under the STEM conditions indicate that the electron density distribution is highly localized to lanthanum and aluminum atomic columns under the experimental conditions, giving rise to localized x-ray emission from these respective columns. The total La L and Al K x-ray counts in Fig. 4.1b are 435 and 135. The x-ray maps are sparsely populated and there are not clear patterns. Using the reference HAADF image (Fig. 4.1c), the {100} lattice planes were overlaid on the map as blue lines in Fig. 4.1b, where the line intersections represent the positions of lanthanum columns (extending into the page), and the centers of the grids represent the aluminum columns. Careful examination indicates that the x-ray distribution (Fig. 4.1b) is not random. In particular, the red dots (La L) are found to be preferentially populated around the crosses (lanthanum columns).

To see the statistical distribution, the La L x-rays on the map were translated into a single unit cell using the lattice-translation operation (details available in Supporting Information), and the resulting map (displayed in 2×2 unit cells) is shown in Fig. 4.1d. It is clear from Fig. 4.1d, that the La L x-ray signals preferentially occupy the corner of the unit cell. The same operation on Al K x-rays by the lattice-translation leads to a map shown in Fig. 4.1e, indicating the Al K x-ray distribution is centered on the center of the unit cell. The map for Al K x-rays (Fig. 4.1e) is considerably noisier owing to fewer x-ray counts available for aluminum atoms. A 3-pixel smoothing of the maps in Figs. 4.1d and 4.1e leads to the images in Figs. 4.1f and 4.1g. Finally, a composite RGB map (La in red, Al in green) (Fig. 4.1h) clearly shows the chemical structure for $LaAlO_3$ crystal in [001] projection.

Attempts have also been made to acquire the EDS dataset at an even shorter acquisition time. Figure 4.1i shows the (La, Al) RGB map obtained from the dataset acquired with only a single frame scan (or a collection time of 0.6 sec) and after undergoing the same data processing described above. Under this condition, the total x-ray counts for La L and Al K in the image are about 159 and 54, respectively. For this short collection time, the chemical map (Fig. 4.1i) is relatively noisy and it would be difficult to recognize the atomic distribution without *a priori* knowledge. Increasing the acquisition time by factor of 3 to 5, though, makes the chemical mapping much clearer as shown in Fig.4.1j, which is obtained with ~8 sec collection.

Statistics play a critical role in the technique described. To verify that the chemical map obtained by this method is indeed representative of the averaged chemical structure, a phenomenological model was developed to simulate the process. Our model simulates a geometrical condition identical to our experiments, i.e., the x-ray

map of 200×200 pixels, and the lattice made of the unit-cells of 17×17 pixels (Fig.4.1b). The model generates random pixel-positions for x-rays to reside within the map and assumes the map to contain both the signal and noise counts. Here we define the signal as the x-ray counts that are generated randomly, but localized around the respective atomic positions within a certain pixel radius. Conversely, the noise counts are distributed randomly across the map regardless of atomic positions. We assume the signal count is localized around the corner of the unit-cell with a radius of 6 pixels (or about 0.13 nm), which was estimated based on current experimental conditions[11], and further assume that N equals to $3S^{1/2}$ where S is the total signal count and N is total noise count. Note that N equals to $S^{1/2}$ is typically used for x-ray counting that obeys Gaussian statistics. Using $N = 3S^{1/2}$ instead is a simple acknowledgment that the noise level under our definition will be higher due to the fact that the TEM specimen is often not ideal and that the presence of an amorphous layer on the top and the bottom surfaces of TEM sample would increase the non-localized counts or the noise.

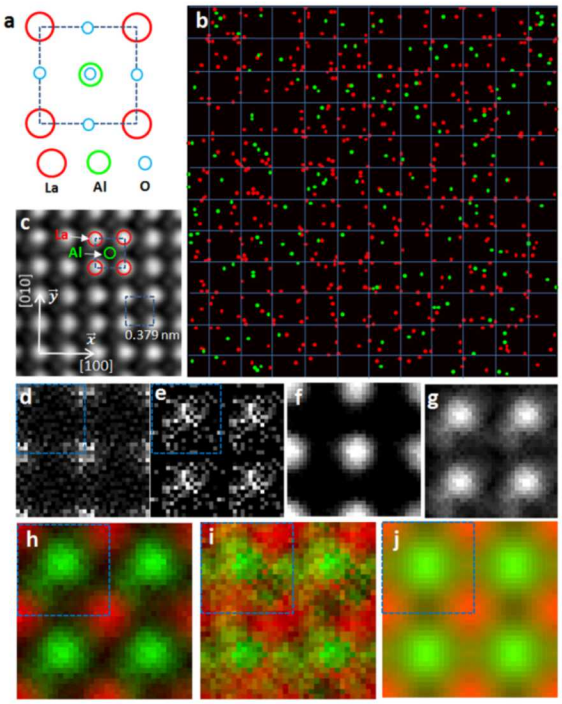

Figure 4.1 Fast STEM EDS atomic-scale chemical mapping achieved with a short collection time. (a) Projected LaAlO3 structure in a [001] direction; (b) raw x-ray count maps of La L (red-dot) and Al K (green-dot), obtained by STEM EDS with a total acquisition of 1.8 sec (the overlaid blue lines show the lattice of LaAlO3 with lanthanum columns at the crosses and aluminum columns at the grid centers); (c) the reference HAADF image obtained simultaneously with EDS mapping (only ¼ shown); (d, e) X-ray count maps (2×2 unit cells shown) for La L, and Al K x-rays, respectively, obtained by the lattice-translation method using the x-ray map in (b); (f, g) obtained by 3-point smoothing of the maps in (d, e); (h) (La, Al) RGB map obtained with maps (f, g); (i) (La, Al) RGB map obtained by STEM EDS with a total acquisition of 0.6 sec; and (j) (La, Al) RGB map obtained STEM EDS with a total acquisition of ~8 sec. The blue dashed square in (a, c, d, e, h, i and j) represents the projected LaAlO3 unit cell in [001].

Using the model, the x-ray maps under various signal and noise conditions were simulated (and lattice-translation was used to extract the averaged count distribution (or chemical map) within the unit cell (Fig.4.2). The modeling shows that if all counts are randomly distributed (i.e., the counts are all noise), the lattice-translation operation cannot produce any useful atomic-scale map (Fig.4.2a). For chemical maps with a total signal *S* of greater 1000, a high-quality chemical map can be obtained (Fig.4.2b). At *S* of 100, the chemical map becomes noisy, but a consistent pattern can always be obtained, and a chemical structure can be derived from the pattern (Fig.4.2c). At *S* of 50 or below, the chemical map (Fig.4.2d) becomes very noisy and less consistent.

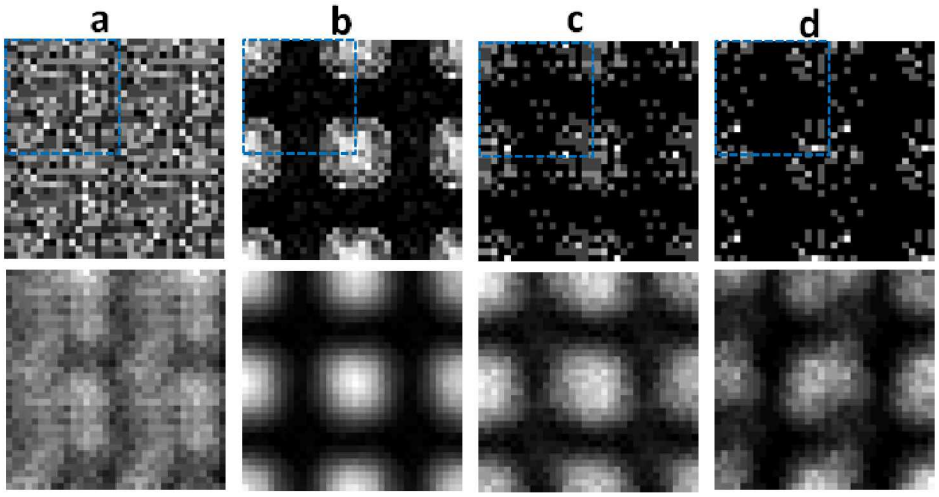

Figure 4.2 Chemical maps extracted from the phenomenological modeling. The chemical maps (2×2 unit cells shown) are obtained by the lattice-translation method using the x-ray count maps simulated by the phenomenological model under various *S* and *N* conditions: (a) *S*=0, *N*=1000; (b) *S*=1000, *N*=100; (c) *S*=100, *N*=30; and (d) *S*=50, *N*=21. The top-panel is the count map, and the bottom-panel is obtained by a 3-point smoothing of the top-panel.

The conditions used for modeling in Figs.4.2b, 4.2c, and 4.2d are similar to the conditions for experimentally obtaining Figs.4.1j, 4.1h and 4.1i, respectively. The result confirms that the chemical map extracted by the lattice-translation approach from the experimental data is a result of the x-ray localization around the atomic columns and is representative of the averaged chemical structure for the crystal. The result also indicates that the minimum x-ray count needed for producing a significant chemical map is around 100 for the given conditions (particularly, the unit size of 0.379 nm × 0.379 nm). Taking the minimum count to be ~100, this requires an acquisition time of ~0.5 sec for lanthanum atoms and ~ 1.5 sec for aluminum atoms under the current experimental conditions. It is likely that the acquisition time can be further shortened by optimizing experimental conditions such as electron probe

current and specimen thickness in such a way that the x-ray emission rate is increased but the localization condition is still satisfied. Note that the acquisition time specifies the number of electrons required for producing the chemical map. For an acquisition time of 1 sec, the number of electrons is ~5.9×10^8 which is obtained by multiplying the probe current (~95 pA for the experimental conditions) with the acquisition time and dividing by the electron charge. The scanned area of 4.46 nm×4.46nm in the probe current of ~95 pA gives rise to overall electron radiation density of 2.9×10^7 electrons/nm^2 for an acquisition time of 1 sec. The size of area scanned can be adjusted according to how sensitive the specimen is to the electron beam radiation. For imaging an extremely radiation sensitive specimen, the electron beam can be scanned over a relatively large crystal area to reduce the overall electron radiation density while keeping the instantaneous dwell time on each pixel short and total acquisition to a fixed time (*e.g.*, 1 sec). In practice, the shortest practical instantaneous dwell is ~10 μsec below which significant signal loss will take place due to the collection electronics. By keeping a total collection time of about 1 sec, this limits the largest scanning frame size to about 320 × 320 pixels or physical area of 7.14 nm × 7.14 nm and the lowest electron radiation density of 1.2 $\times10^7$ electrons/nm^2 under the current experimental conditions.

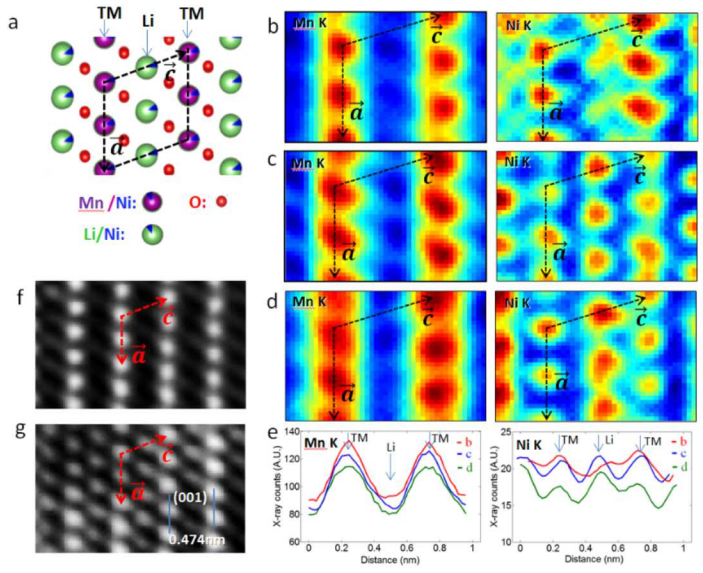

Figure 4.3 Time-resolved atomic-scale chemical imaging study of the phase transformation in $Li[Li_{0.2}Ni_{0.2}Mn_{0.6}]O_2$ (LNMO). (a) Projected LNMO structure in [010] direction; (b-d) x-ray chemical maps of Mn K (left) and Ni K (right), obtained by using the lattice-translation method from three EDS spectral imaging datasets acquired sequentially from the same area (200×300 pixels, or 4.46 nm×6.69 nm), with a collection time of ~4.5 sec each; (e) X-ray line-profiles for Mn K (left) and Ni K (right) obtained from chemical maps in (b-d); (f) and (g): STEM HAADF images of the LNMO before (f) and after (g) the chemical mapping acquisition. LNMO has a monoclinic unit cell (a=0.4926 nm, b=0.8527 nm, c=0.5028nm, and β=109.22°) with space group $C2/m$. Vectors $\vec{a}$ *and* $\vec{c}$ indicate the a- and c-axis of the unit cell.

While the study of $LaAlO_3$ provides compelling evidence of the feasibility of the approach, we further expand the technique to study the dynamic phase transformation in a highly beam-sensitive layered lithium transition-metal oxide, particularly, LNMO. The high specific-capacity of layered lithium transition-metal oxides (~250 mAh/g)[13-15] makes them attractive as cathodes for lithium batteries, but they suffer gradual voltage fade and irreversible capacity loss upon charge-discharge cycling. These problems are attributed to a permanent, irreversible phase transformation on LNMO surfaces during electrochemical charge-discharge cycling[17-20]. High-energy electron beams have also been shown to induce radiation-mediated phase transformations[21-22], identical to those reported during the charge-discharge cycling due to similar point defect environments (*i.e.*, lithium and oxygen vacancies) present in the two conditions[22]. Although recent reports have described the "before and after" conditions of this transformation, the long acquisition times required for atomic-scale mapping have prevented examination of the critical local transient structure involved in the transformation. With this new rapid mapping technique, we can capture the time-resolved evidence of atomic movement in this structural transformation.

LNMO used in this study has a Li_2MnO_3 structure, which has a monoclinic unit cell (a=0.4926 nm, b=0.8527 nm, c=0.5028 nm, and β=109.22°) with space group $C2/m$[23-24]. The structure exhibits a layered structure composed of repeating TM, oxygen and lithium layers (Fig.4.3a). In the lithium layers, presence of a small percentage (~4%) of nickel atoms has also been proposed based on x-ray diffraction and neutron diffraction measurements[14-15]. Three sequential EDS datasets were taken from the same specimen area with a collection time of ~4.5 sec for each dataset. The spectral imaging was acquired at 200×300 pixels, corresponding to a physical frame size of 4.46 nm×6.69 nm. The collection time of ~4.5 sec corresponds to accumulation of 5 frames (~0.9 sec per frame with an instantaneous dwell time on each pixel of 15 μsec). Chemical maps of Mn K and Ni K x-rays extracted by the lattice-translation method from the three datasets are shown in Figs. 4.3b, 4.3c, 4.3d, respectively. The difference amounts to approximately 4.5 seconds of electron exposure. The chemical maps (Fig. 4.3b), obtained without pre-acquisition electron-beam exposure, show the chemical structure that is most-closely related to the initial structure reported[14-15], *i.e.*, the manganese and nickel atoms reside within the TM layers at pre-determined atomic sites. The maps (Fig. 4.3c) from the area which has been exposed with the electron beam (a total electron radiation density of ~8.8×10^7 electrons/nm^2) during the first dataset collection show that the manganese atoms retained the lattice positions in the TM layers, but the majority of nickel atoms in the TM layers jumped into the lithium sites during the beam exposure. Further electron beam irradiation (a total pre-acquisition electron radiation density of ~1.77×10^8 electrons/nm^2) drove additional nickel atoms into the lithium sites, but still produced no significant changes of manganese occupancy in the TM layer (Fig. 4.3d). This observation indicates that the phase transformation progresses as nickel atoms jump preferentially (relative to manganese atoms) into the lithium sites once the sites are vacated. This is the first clear, atomic-scale evidence of this phenomenon, and was uniquely generated by this fast mapping technique. Based on the observed atomic mobility in this short electron irradiation time, it is clear that traditional mapping processes, requiring 100X more

electron exposure, would miss this subtle, but important phenomenon. The STEM HAADF images in Figs. 4.3f and 4.3g, taken before and after the three spectral imaging series, indicate that the phase transformation did indeed take place during electron radiation, and that the TM atoms (clearly nickel based on chemical images in Figs.4.3c and 4.3d) jumped into the lithium layers.

It is important to note that the phase transformation took place continuously during the spectral imaging acquisition. The time-series of the chemical structure obtained represents the averaged structure during the data acquisition. Due to dynamic nature of the phase transformation, the atoms can be at the off-site positions during the transition. With that in mind, the off-lattice-site intensity showing in the Ni K map (right-map in Fig. 4.3b) could be real. This distribution is also visible in the x-ray line-profile (red-line, right-panel of Fig. 4.3e), which exhibits a shoulder-like peak away from the lithium layer position in the profile obtained from Fig. 4.3b. In addition, the line-profile (Fig. 4.3e) further indicates that although the manganese atom remains in the TM layer, its EDS peak broadens gradually during the phase transformation. This observation indicates an increased range of atomic motion about the lattice sites, likely due to the presence of the oxygen vacancies also induced during electron-beam irradiation. Our observation that nickel atoms preferentially move into the vacated lithium sites during the phase transformation corroborates previous observations that show presence of excess nickel on surfaces of LNMO particles after electrochemical charge-discharge cycling[25-26]. The novel approach described here provides unique insights to explain this technically important phenomenon.

Finally, although we present here a promising approach to studying beam-sensitive materials or dynamic phenomena in crystalline materials, it should be noted the technique does have some limitations. It is applicable only to crystalline materials with a long range ordering (> few nm), and provides an averaged chemical structure from areas of a few 10s nm^2 at the atomic-scale. It can't be applied to investigate individual defect structures such as a single dislocation. Nevertheless, the averaged area of few 10 nm^2 is much smaller than that of other existing time-resolved structural characterization technique such as x-ray diffraction[12]. The technique, in addition to being able to probe local chemical structure, is a real-space approach which makes the data interpretation straightforward. It is also possible to distinguish chemical elements that have similar atomic numbers (*e.g.,* manganese, nickel in LNMO) since unique chemical signals are used for identification of the atomic columns. Furthermore, this technique is capable of deriving an averaged point defect distribution in the crystalline materials for applications such as determination of dopant sites since the dopants are typically localized to specific and unique sites within the crystal so long as the dopant concentration is above the EDS detection limit.

3.4. Summary

In summary, our results clearly demonstrate that atomic-scale chemical imaging can be achieved with an acquisition time of less than a few seconds using STEM EDS.

The technique utilizes x-ray localization effect and a lattice-vector translation to derive an averaged atomic-scale chemical structure from a crystal area of few 10 nm^2, effectively reducing the acquisition time by more than 100X. By applying the technique to the study of the phase transformation in a LNMO lithium-ion cathode material, we uniquely revealed a previously unknown structural transformation mechanism involving the preferred jumping of nickel atoms (relative to manganese atoms) from the TM layers to the lithium layers. This development opens up exciting new possibilities for direct, time-resolved atomic-scale mapping of crystal structures and enables unprecedented investigations of atomic-scale behaviors in dynamic materials.

REFERENCES

References for Section #1

[1] J. Mannhart and D.G. Schlom, Science 327, 1607 (2010).
[2] P. Zubko, S. Gariglio, M. Gabay, P. Ghosez, and J.-M. Triscone, Annu. Rev. Condens. Matt. Phys. 2, 141 (2011).

References for Section #2

[1] Apalkov, D.; Dieny, B.; Slaughter, J.M. *Proceedings of the IEEE* **2016**, 104, 1796-1830.
[2] Akerman, J. *Science* **2005**, 308, 508–510.
[3] MacManus-Driscoll, J.L.; et al. *Nat. Mater.* **2008**, 7, 314 - 320.
[4] Narayan J. Metallurgical and Materials Transactions B **2005**, 36, 5-22.
[5] Chen, A.; et al. *Adv. Funct. Mater.* **2011**, 21, 2423-2429; Chen, A.; et al, *Appl. Phys. Lett.* **2013**, 102, 093144.
[6] Urushibara, A.; et al. *Phys. Rev. B* **1995**, 51, 14103-14109.
[7] Li, L.; Richter C.; Mannhart, J.; Ashoori, R.C. *Nat. Phys.* **2011**, 7, 762–766.
[8] Hwang, H.Y.; Cheong, S.-W.; Ong, N.P.; Batlogg, B. *Phys. Rev. Lett.* **1996**, 77, 2041-2044 (1996).
[9] Brataas, A.; Kent, A.D.; Ohno, H. *Nat. Mater.* **2012**, 11, 372–381.
[10] Jansen, R. *J. Phys. D: Appl. Phys.* **2003**, 36, R289-R308.
[11] Wang, W.-G.; Li, M.; Hageman, S.; Chien, C.L. *Nat. Mater.* **2012**, 11, 64-68.
[12] Chiba, D.; et al. *Nature* **2008**, 455, 515-519.
[13] Negulyaev, N.N.; Stepanyuk, V.S.; Hergert, W.; Kirschner, J. *Phys. Rev. Lett.* **2011**, 106, 037202.
[14] Merodio, P.; Kalitsov, A.; Chshiev, M.; Velev, J. *Phys. Rev. Applied* **2016**, 5, 064006.
[15] Pan, H.; et al. *Phys. Rev. Lett.* **2007**, 99, 127201.

References for Section #3

[1] J. L. MacManus-Driscoll, P. Zerrer, H. Wang, H. Yang, J. Yoon, S. R. Foltyn, M. G. Blamire, and Q. X. Jia, Nat. Mater. 7, 314 (2008).
[2] J. Mannhart and D.G. Schlom, Science 327, 1607 (2010).
[3] P. Zubko, S. Gariglio, M. Gabay, P. Ghosez, and J.-M. Triscone, Annu. Rev. Condens. Matt. Phys. 2, 141 (2011).
[4] J.M.D. Coey, M. Viret, and S. von Molnar, Adv. Phys. 48, 167 (1999).
[5] V. Kiryukhin, D. Casa, J.P. Hill, B. Keimer, A. Vigliante, Y. Tomioka, and Y. Tokura, Nature 386, 813 (1997).
[6] A. Asamitsu, Y. Tomioka, H. Kuwahara, and Y. Tokura, Nature 388, 50 (1997).
[7] A. Baikalov, Y. Q. Wang, B. Shen, B. Lorenz, S. Tsui, Y. Y. Sun, Y. Y. Xue, and C. W. Chu, Appl. Phys. Lett. 83, 957 (2003).
[8] Zheng Yang, Changhyun Ko, and Shriram Ramanathan, Annu. Rev. Mater. Res. 41, 337 (2011).
[9] C. Moreno, C. Munuera, S. Valencia, F. Kronast, X. Obradors, and C. Ocal, Nano Lett. 10, 3828 (2010).
[10] B.S. Kang, H. Wang, J.L. MacManus-Driscoll, Y. Li, Q.X. Jia, I. Mihut, and J.B. Betts, Appl. Phys. Lett. 88, 192514 (2006).
[11] A.P. Chen, Z.X. Bi, C.F. Tsai, J.H. Lee, Q. Su, X.H. Zhang, Q.X. Jia, J.L. MacManus-Driscoll, and H.Y. Wang, Adv. Funct. Mater. 21, 2423 (2011).

[12] H. Zheng, J. Kreisel, Y.H. Chu, R. Ramesh, and L. Salamanca-Riba, Appl. Phys. Lett. 90, 113113 (2007).
[13] Z. Wang, Y. Li, R. Viswan, B. Hu, V.G. Harris, J. Li, and D. Viehland, ACS Nano 7, 3447 (2013).
[14] N. Dix, V. Skumryev, V. Laukhin, L. Fabrega, F. Sanchez, and J. Fontcuberta, Mat. Sci. and Eng. B 144, 127 (2007).
[15] P. Lu et al., Sci. Rep. 4, 3945 (2014).
[16] A.P. Chen, Z. Bi, C.-F. Tsai, J.H. Lee, Q. Su, X. Zhang, Q.X. Jia, J.L. MacManus-Driscoll, and H.Y. Wang, Adv. Funct. Mater. 21, 2423 (2011).
[17] H.Y. Hwang et al PRL 77, 2041 (1996)
[18] Wonyoung Lee, Jeong Woo Han, Yan Chen, Zhuhua Cai, and Bilge Yildiz, J. Am. Chem. Soc. 135, 7909 (2013).

References for Section #4

[1] Browning, N.D.; Chisholm, M.F.; Pennycook, S.J. Nature 1993, 366, 143.
[2] Kimoto, K.; Asaka, T.; Nagai, T.; Saito, M.; Matsui, Y., Ishizuka, K. Nature 2007, 450, 702.
[3] Muller, D.A.; Fitting Kourkoutis, L.; Murfitt, M.; Song, J.H.; Hwang, H.Y.; Silcox, J.; Dellby, N.; Krivanek, O.L. Science 2008, 319, 1073.
[4] Allen, L.J.; Findlay, S. D.; Lupini, A.R.; Oxley, M. P.; Pennycook, S.J. Phys. Rev. Lett. 2003, 91, 105503.
[5] Allen, L. J.; D'Alfonso, A.J.; Freitag, B.; Klenov, D. O. MRS Bulletin 2012, 37, 47-52.
[6] Bosman, M.; Keast, V.J.; Garcia-Munoz, J.L.; D'Alfonso, A.J.; Findlay, S.D.; Allen, L.J. Phys. Rev. Lett. 2007, 99, 086102.
[7] Watanabe, M.; Kanno, M.; Okunishi, E. JEOL News 2010, 45, 8-15.
[8] D'Alfonso, A.J. ; Freitag, B. ; Klenov, V. ; Allen, L.J. Phys. Rev. B 2010, 81, 100101.
[9] Chu, M.W.; Liou, S.C.; Chang, C.P.; Choa, F.S.; Chen, C. H. Phys. Rev. Lett. 2010, 104, 196101.
[10] Lu, P.; Zhou, L.; Kramer, M.J.; Smith, D.J. Sci. Rep. 2014, 4, 3945.
[11] Lu, P.; Romero, E.; Lee, S.; MacManus-Driscoll, J. L.; Jia, Q. Microsc. Microanal. 2014, 20, 1782-1790.
[12] Gras, C.H.; Charlot., F.; Gaffet, E.; Bernard, F.; Niepce, J.C. Acta mater. 1999, 47, 2113-2123.
[13] Zhang, X.; Xu, R.; Li, L.; Yu, C.; Ren, Y.; Belharouaka, I. J. Electrochem. Soc. 2013, 160, A1079-A1083.
[14] Fell, C.R.; Carroll, K. J.; Chi, M.; Meng, Y.S. J. Electrochem. Soc. 2010, 157, A1202-A1211.
[15] Lu, Z.H.; Beaulieu, L. Y.; Donaberger, R.A.; Thomas, C.L.; Dahn, J. R.
J. Electrochem. Soc. 2002, 149, A778-A791.
[16] Cowley, J.M. Diffraction Physics, 2nd edition, Elsevier Science Publishing, New York, 1984.
[17] Gu, M.; Belharouak, I.; Zheng, J.M.; Wu., H.M.; Xiao, J.; Genc, A.; Amine, K.; Theyuthasan, S.; Baer, D.R.; Zhang, J-G.; Browning, N.D.; Liu, J.; Wang, C.M. ACS Nano 2013, 7, 760-767.
[18] Boulineau, A.; Simonin, L.; Colin, J.-F.; Bourbon, C.; Patoux, S. Nano Lett. 2013, 13, 3857-3863

[19] Xu, B.; Fell, C. R.; Chi, M.; Meng, Y. S. Energy & Environmental Science 2011, 4, 2223-2233.
[20] Lin, F. Markus, I.M.; Nordlund, D.; Weng, T-C.; Asta, M.D.; Xin, H.L.; Doeff, M.M. Nat. Commun. 2014, 5, 3529-3537.
[21] Lin, F.; Markus, I. M.; Doeff, M. M.; Xin, H.L. Sci. Rep. 2014, 4, 5694.
[22] Lu, P.; Yan, P.F.; Romero, E.; Spoerke, E.D.; Zhang, J.-G.; Wang, C.-M. Chem. Mater. 2015, 27, 1375-1380.
[23] Strobel, P; Labert-Andron, B. J. Solid State Chem. 1988, 75, 90.
[24] Jarvis, K.A.; Deng, Z.Q.; Allard, L.F.; Manthiram, A. Ferreira, P.J. Chem. Mater. 2011, 23, 3614-3621.
[25] Gu, M.; Belharouak, I.; Genc, A.; Wang, Z.G.; Wang, D.P.; Amine, K.; Gao, F.; Zhou, G.W.; Theyuthasan, S.; Baer, D.R. et al.; Nano Lett. 2012, 12, 5186-5191.
[26] Yan, P.; Nie, A.; Zheng, J.M.; Zhou, Y.G.; Lu, D. P.; Zhang, X.F.; Xu, R.; Belharouak, I.; Zu, X.T.; Xiao, J. et al. Nano Lett. 2015, 15, 514-522.

DISTRIBUTION

4	Lawrence Livermore National Laboratory Attn: N. Dunipace (1) P.O. Box 808, MS L-795 Livermore, CA 94551-0808		
1	MS0359	Jerry A. Simmons	1000
1	MS0359	D. Chavez, LDRD Office	1911
1	MS1002	Daniel L. Barton	6520
1	MS1086	Wei Pan	1867
1	MS1086	Stephen R. Lee	1876
1	MS1411	Ping Lu	1819
1	MS1421	Arthur J. Fischer	1867
1	MS0899	Technical Library	9536 (electronic copy)

Sandia National Laboratories